Chemical identification of new particle formation and growth precursors through positive matrix factorization of ambient ion measurements

S1 Fitting of binPMF peaks

In order to evaluate the error introduced by the binPMF and peak-fitting process, synthetic peaks were generated and analyzed. First, Gaussian peaks at selected positions between *m/z* 200 and 550 were generated in time-of-flight (ToF) space. Peak widths were equal to real peaks observed at the selected *m/z*. The peaks were sampled in ToF space at the same interval as the APi-ToF data acquisition. The ToF space to *m/z* space transformation was calculated as:

$$m/z = \left(\frac{(ToF - p1)}{p2}\right)^2 \quad \text{(S.1)}$$

where p1 and p2 are the fit parameters selected for the simulation and ToF is the time of flight (ns). This function was selected for the simulated data because it was found to the best fit function for real data and was used to fit both positive and negative mode data throughout the campaign. "True" values for p1 and p2 were selected for the simulation. To simulate an upper limit estimate on error in the mass calibration and its impact on the binPMF results, pairs of p1 and p2 values were randomly selected from the set of p1 and p2 values fit from the ambient data using Tofware. Because p1 and p2 do not vary independently, each pair of values consisted of parameters calculated for the same time point in the calibration. This is an upper estimate of our error because it assumes that all shifts in mass calibration contribute error, but there are real shifts in p1 and p2 that result from temperature changes, drift within the instrument, and other factors. Following the ToF to *m/z* space transformation, the synthetic peaks in *m/z* space were binned using the same bins and bin widths used for binPMF and fit with a Gaussian to determine the peak center. Error introduced by the *m/z* calibration was determined using a Monte Carlo method to randomly select many sets of p1 and p2. Root mean squared errors introduced by this method were approximately 50 ppm for both positive and negative mode data. The simulation was also repeated using only the "true" fit parameters to determine whether error in the peak positions originated from simulated error in the mass calibration or from the binning and fitting procedure. Error was negligible (<<1 ppm) when using the "true" fit parameters, suggesting that most error is from the mass calibration and not the fitting procedure. Peak broadening was also evaluated. Peaks may be broadened both by the procedure of binning and fitting peaks to bins and by shifts in the mass calibration throughout the campaign. Figure S1 shows the comparison between the peak in a 15-minute average mass spectrum at *m/z* 487 and the Gaussian peak fit to the bins at that mass. Minimal broadening is observed. It should also be noted that peak widths have no direct implications for the conclusions of this work. Peak shape was also investigated. Figure S2 compares the high-resolution peak shape calculated in Tofware and a Gaussian

peak shape fit to binPMF peaks. Although minor differences in peak shape are apparent, the shapes are broadly similar and, as with peak widths, peak shapes do not directly impact our results.

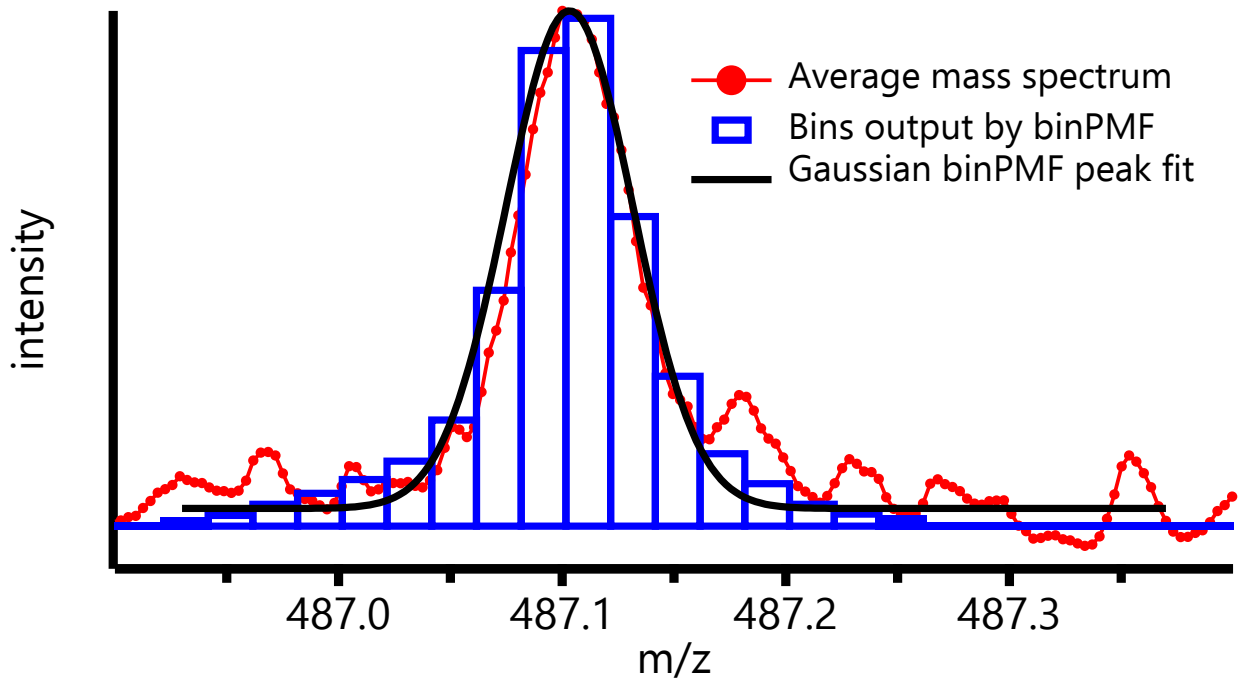

Figure S1: comparison of 15-minute average measured mass spectrum, binPMF binned signal, and Gaussian peak fit. Each bin is centered on the *m/z* value at the midpoint of the bin. The averaging time was 15 minutes.

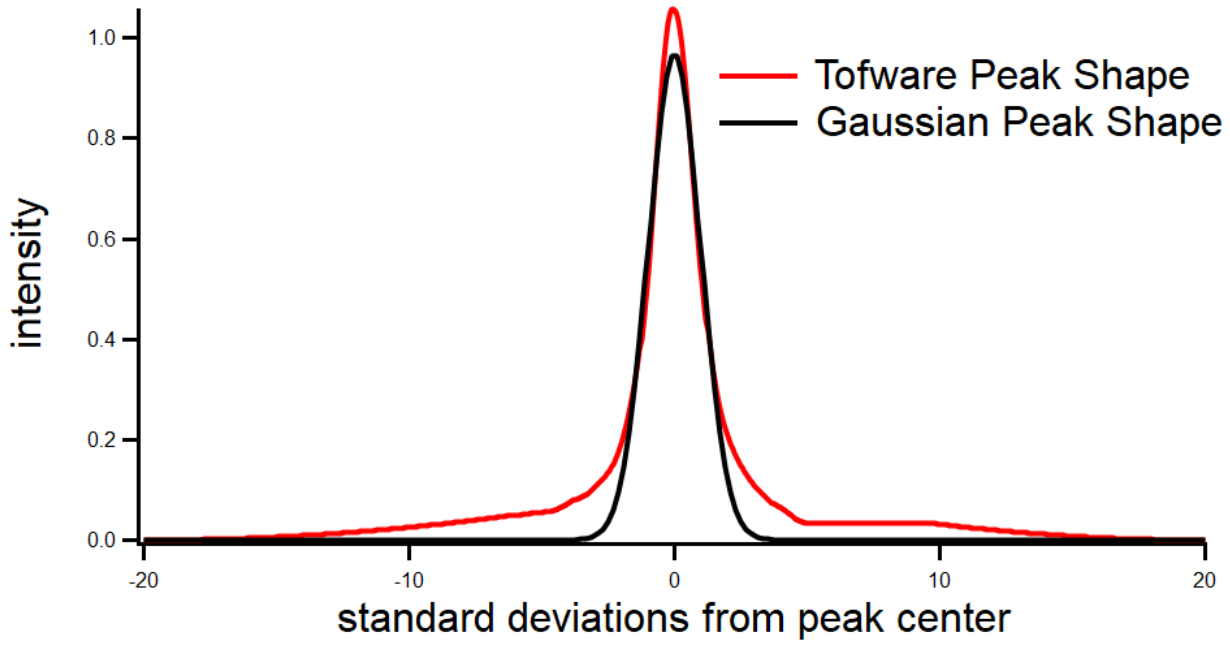

Figure S2: Comparison of Tofware peak shape and Gaussian peak shape.

S2 binPMF error estimation

Electronic noise contributes more to error than counting statistics because of the low signal-to-noise of APi- ToF data. Thus, our initial investigation of error used values independent of signal intensity. We investigated two alternative error estimation methods in addition to the one described in the main text. In one of these we used only the very high *m/z* bins where no peaks were observed. For both positive and negative datasets no peaks were observed beyond *m/z* 700 and all *m/z* 700-1400 were used to estimate error. As with the technique described in the main text, the noise in this region was binned in the same manner as the signal at lower *m/z*. The standard deviation was then calculated for each noise bin throughout the campaign. All standard deviations for bins in the range *m/z* 700-1400 were then averaged. This results in one error value for all *m/z* and all time points.

We also investigated time-dependent error calculated using the high *m/z* noise bins. With this method one error value was calculated for all *m/z*, but it was allowed to vary over time. The standard deviation of all bins at *m/z* 700-1400 was calculated for each time point. This value was then used as the error for every *m/z* at that time point. These differing error estimation techniques produced similar distributions of error values (Fig. S3) with individual values within an order of magnitude of each other. The different error estimates did not result in significantly different binPMF solutions. We found PMF solutions to be insensitive to exact error values for error values of the correct order of magnitude.

Signal-to-noise ratios (SNRs) were not used to weight final binPMF results. While we did perform some PMF calculations with downweighting of low SNR bins, the solutions were very similar to those calculated without weighting. We found that baseline correction was far more important than signal weighting in achieving binPMF solutions that are not obfuscated by excess noise. With poor baseline correction, a factor containing mostly noise was produced. Bins that did not contain chemical information were sorted into the noise factor, and the intensity of the factor varied to capture the drift in the baseline. With better baseline correction electronic noise was subtracted from the spectra prior to binning and all the binPMF factors contained chemically meaningful information. Since bins lacking in chemical information were addressed by the baseline correction, we determined that weighting was not necessary for our analysis.

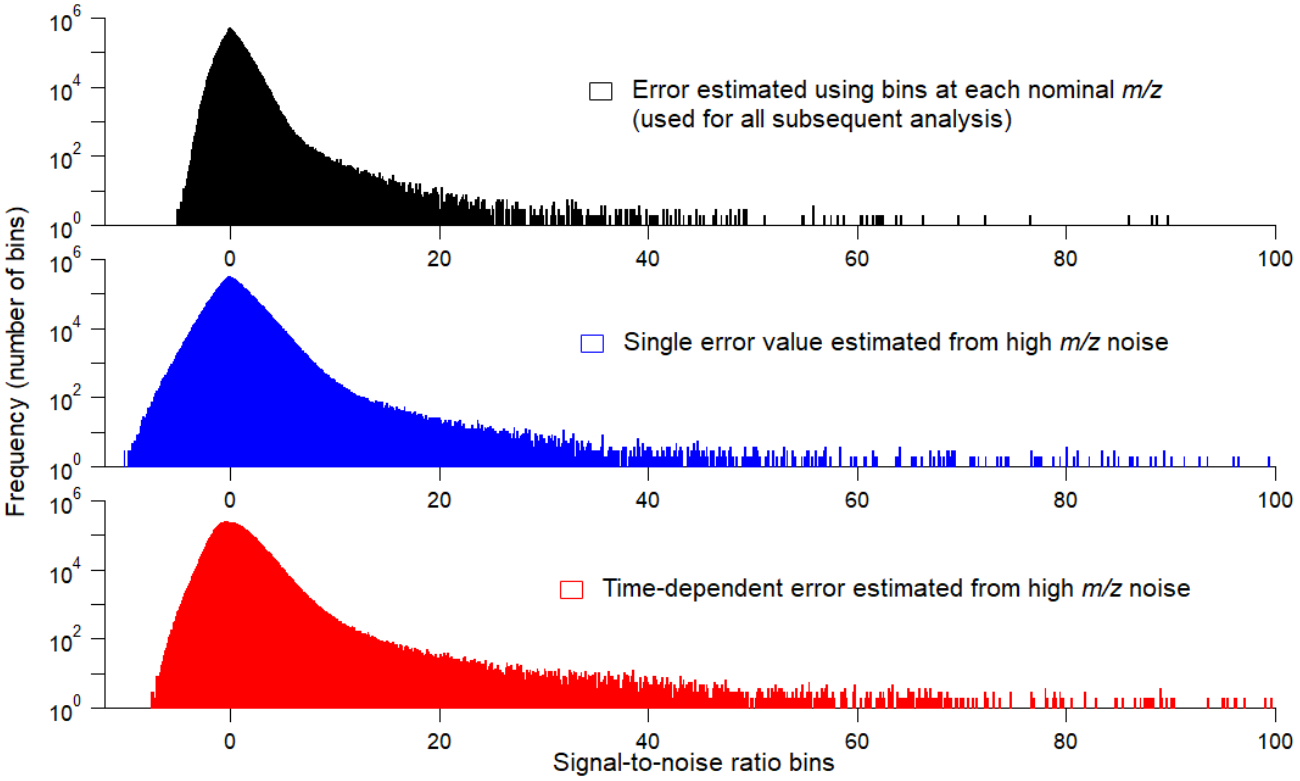

Figure S3: Histograms of the SNR calculated for each bin at each time point using the three different error estimation techniques.

S3 Sulfuric acid proxy calculation

The sulfuric acid concentration proxy was calculated using the method described by Mikkonen et al. (2011) using the formula:

$$[H_2SO_4] = 8.21 \times 10^{-3} \times k \times Radiation \times [SO_2]^{0.62} \times (CS \times RH)^{-0.13} \quad \text{(S2)}$$

where k is the effective rate coefficient of sulfur dioxide oxidation by hydroxyl radicals in cm^3/molec·s, radiation is a measurement of shortwave radiation (0.4-4 μm) in W/m^2, $[SO_2]$ is the measured concentration of sulfur dioxide in molec/cm^3, CS is the condensation sink in s^{-1}, and RH is the relative humidity. The constant is an empirical value derived from fitting measured sulfuric acid data. While Mikkonen et al. (2011) fit data from several different campaigns to calculate a constant that should be applicable under a wide variety of conditions, we cannot be certain that this value effectively reproduces the sulfuric acid concentration at SGP. Regardless, our sulfuric acid proxy was used only to understand the trends in sulfuric acid, and the absolute magnitude of the sulfuric acid concentration is not relevant to our conclusions. The effective rate coefficient of sulfur dioxide oxidation, k, was calculated by:

$$k = \frac{A \cdot k_3}{(A+k_3)} exp\left\{k_4\left[1 + \log_{10}\left(\frac{A}{k_3}\right)^2\right]^{-1}\right\} \quad \text{(S3)}$$

$$A = k_1[M] \cdot \left(\frac{300}{T}\right)^{k_2} \quad \text{(S4)}$$

where $k_1 = 4\times10^{-31}$, $k_2 = 3.3$, $k_3 = 2\times10^{-12}$, $k_4 = 0.8$, [M] is the density of air in molec/cm^3, and T is the temperature in Kelvin (Mikkonen et al., 2011). The condensation sink was calculated according to the equation:

$$CS = 2\pi D \sum_i D_{pi}\beta_i N_i \quad \text{(S5)}$$

where D is the diffusion coefficient of sulfuric acid in m^2/s, D_{pi} is the diameter in m of particles in class size i, β_i is the Fuchs-Sutugin correction factor, and N is the number concentration of particles in number/m^3. Measurements of SO_2, particle size distribution, RH, radiation, and the parameters required to calculate the condensation sink are made routinely at the site (Trojanowski, 2016; Zhang, 1997).

S4 Negative binPMF solution selection

Compared to the four-factor solution presented in the main text, the three-factor solution (Fig S4), essentially combines the "sulfur species factor" and the "low *m/z* nitrate factor." While the sulfuric acid dimer is still represented fairly well by this solution, nearly every other daytime sulfur species at low *m/z* (including bisulfate, bisulfate clustered with water, sulfur pentoxide) has a very high residual and is not well-captured. Adding another factor allows the low *m/z* sulfur species to be sorted into a separate factor that reflects their behavior. In the five-factor solution (Fig S5), only the high *m/z* nitrate factor changes significantly. It is split into two factors with very similar mass spectra and diel behavior. One of the two new factors has a time series nearly identical to the time series of the high *m/z* nitrate factor except for a few short periods where it dips nearly to zero, and the other new factor has a time series that is nearly always close to zero except for brief spikes which correspond to the dips in the other factor (i.e. the sum of the two new time series is very similar to the time series of the high *m/z* nitrate factor in the four-factor solution). There does not appear to be any chemical explanation for these spikes, and they are likely due to small shifts in the mass calibration throughout the campaign. Combined with the similarity of the spectra, the unusual behavior of the time series implies that the splitting of the high *m/z* nitrate factor into two new factors has no chemical significance. Therefore, a fifth factor is not included and the four-factor solution is selected for further analysis.

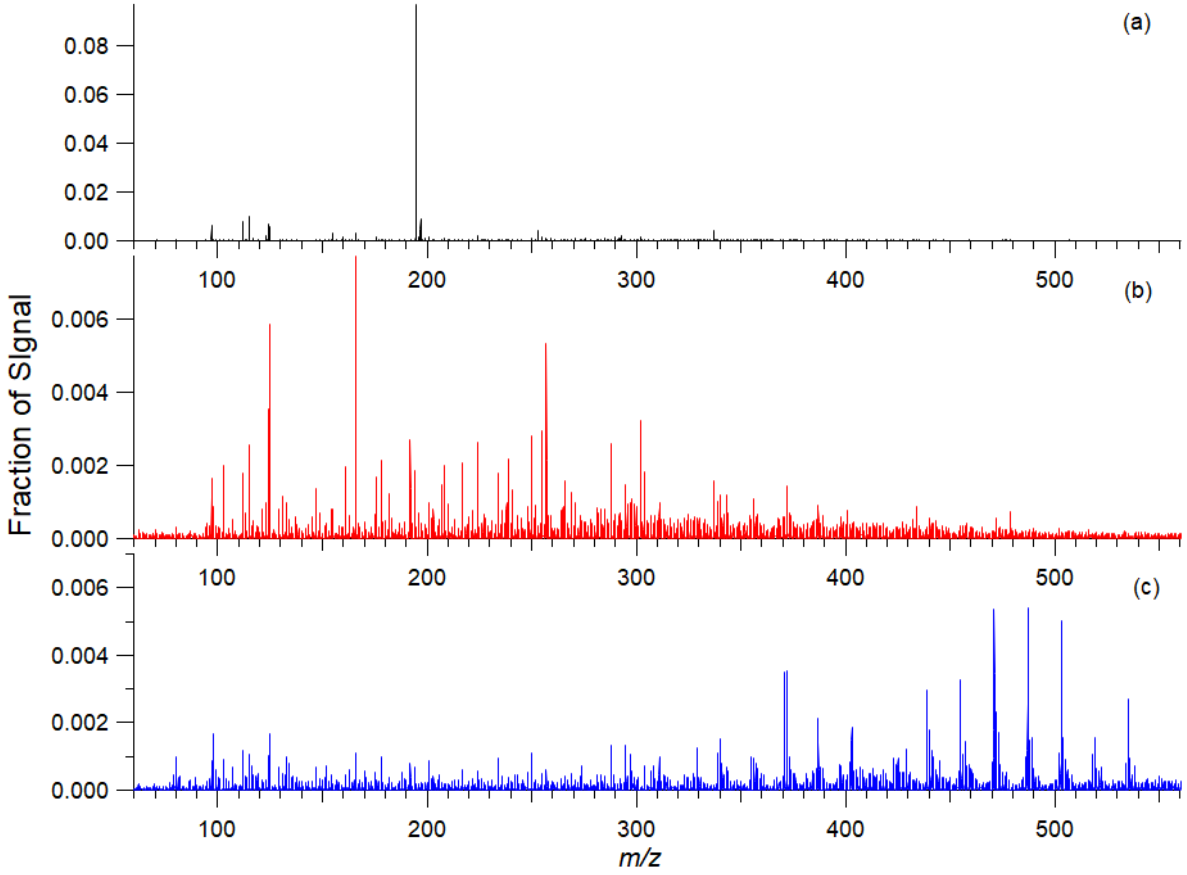

105 **Figure S4: Mass spectra of the factors in the three-factor negative binPMF solution.**

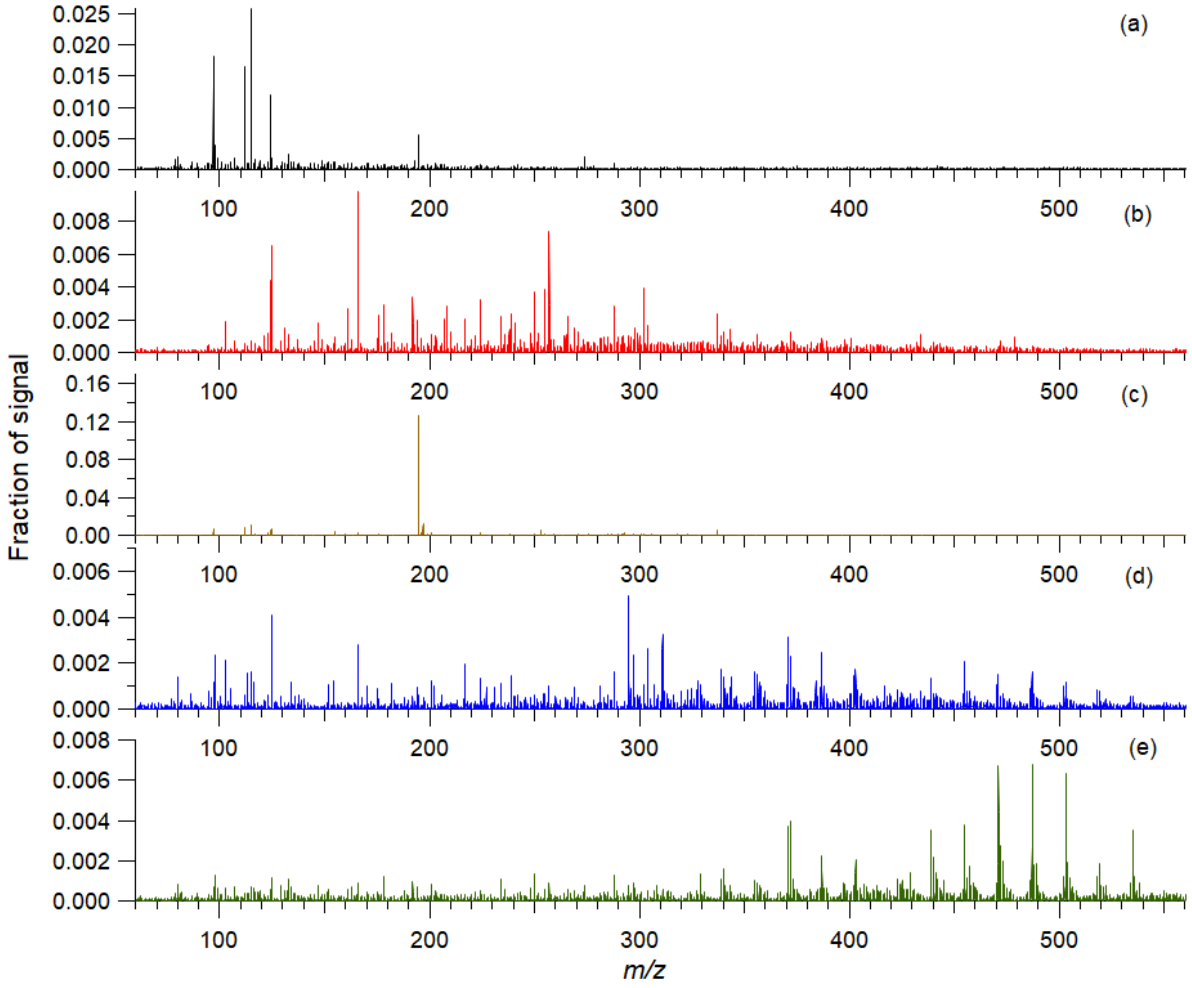

Figure S5: Mass spectra of the factors in the five-factor negative binPMF solution.

S5 Time series of negative binPMF factors

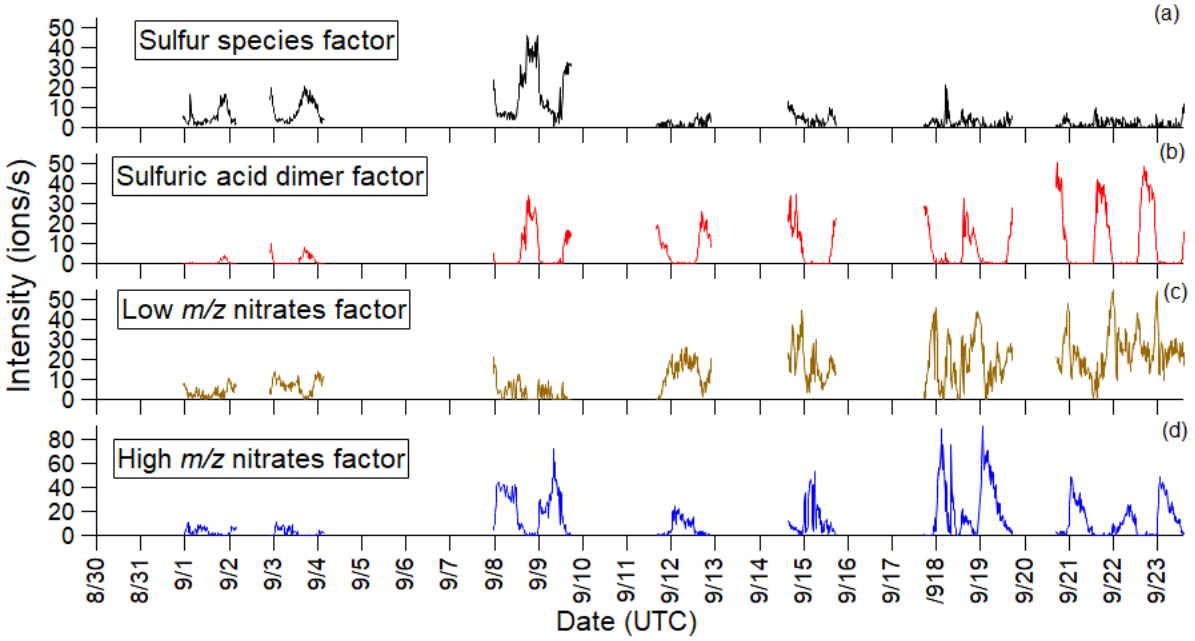

Figure S6: Time series of the four-factor negative binPMF solution throughout the campaign – (a) sulfur species factor, (b) sulfuric acid dimer factor, (c) low *m/z* nitrates factor, and (d) high *m/z* nitrates factor.

S6 Diel profiles of organosulfates

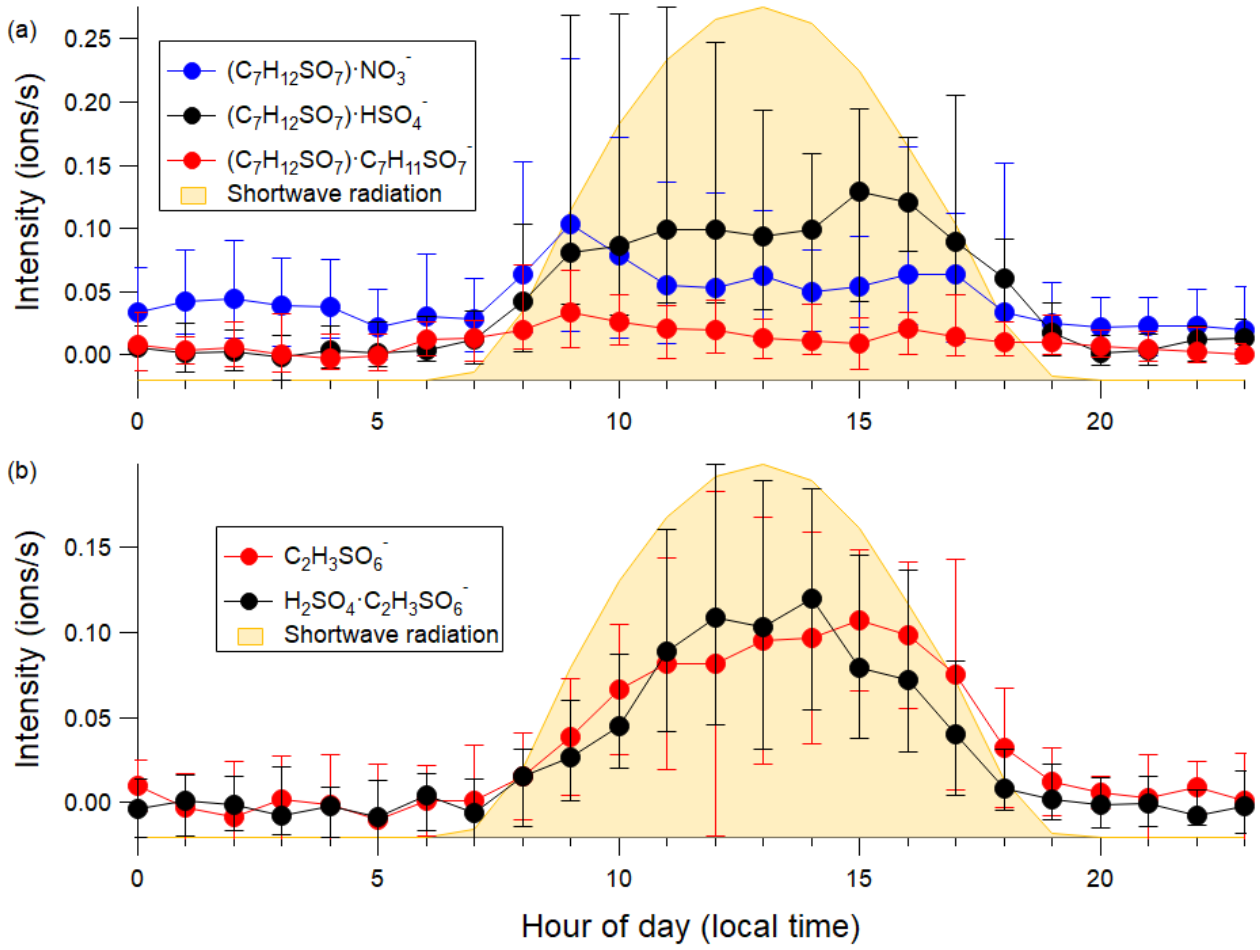

Figure S7: Diel profiles of selected organsulfates (a) Clusters of $C_7H_{12}SO_7$ (C7) with various anions and, (b) glycolic acid sulfate (GAS, $C_2H_3SO_6^-$) and its cluster with bisulfate.

S7 Time series of selected PTRMS ions

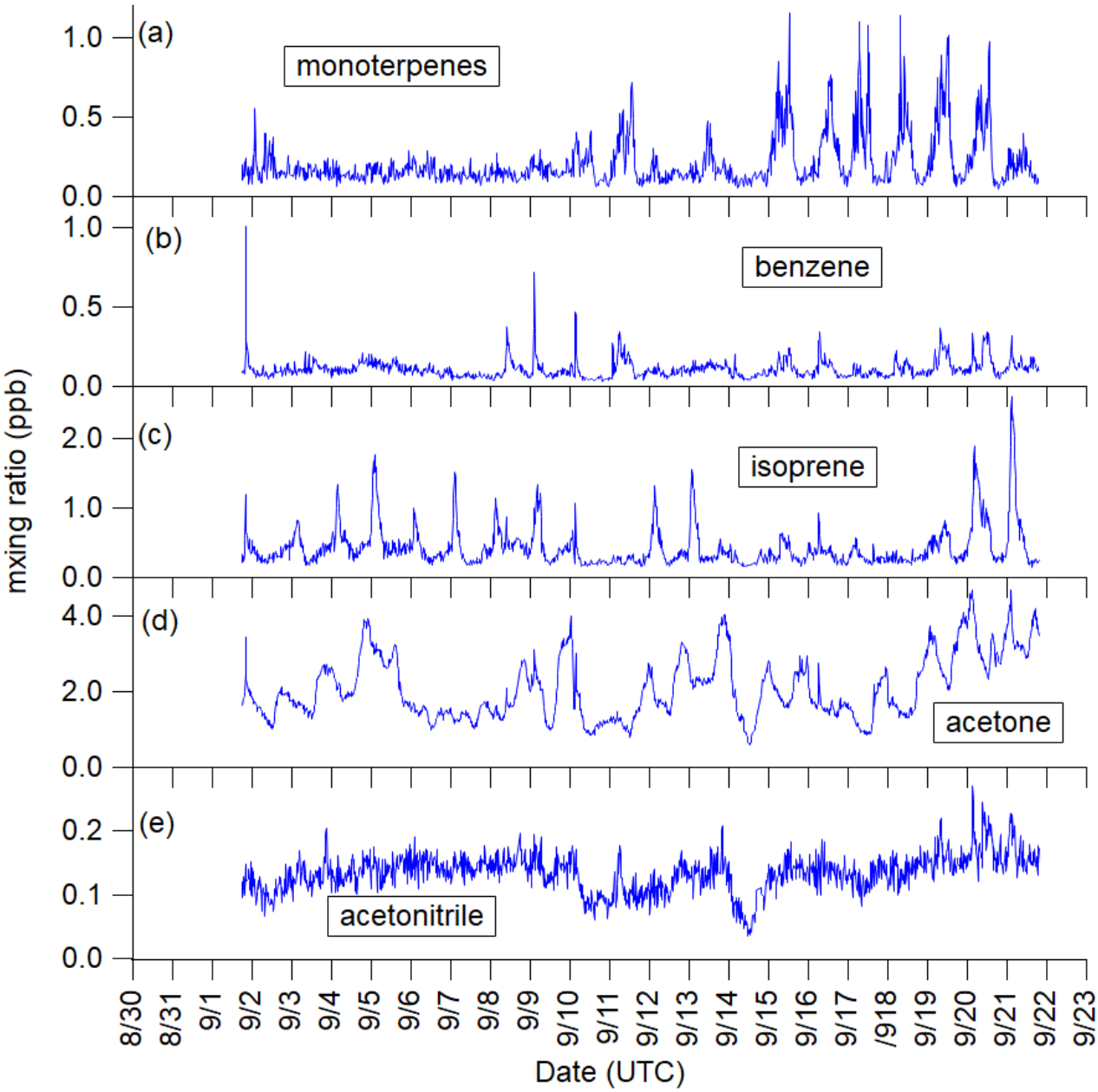

Figure S8: Time series of selected trace gases measured by the proton transfer reaction mass spectrometer through the campaign – (a) monoterpenes, (b) benzene, (c) isoprene, (d) acetone, and (e) acetonitrile.

The PTRMS measurements are external tracers that substantiate the changes observed in binPMF factors. The time series of monoterpenes measured by the PTRMS (Fig. S7a) shows a strong increase in the second half of the campaign. Several binPMF

factors in both the negative and positive mode show similar increases midway through the campaign. Although it does not coincide exactly with the increases in intensity of binPMF factors, the increase in monoterpenes measured by the PTRMS suggests that the changes in the intensity of the binPMF factors is not due to instrument artefacts. The instrument did become clogged at a similar point in the campaign (13 September). The primary effect of a clog, however, would be to reduce measured signal rather than alter the signal composition. Furthermore, any change in composition induced by a clog would likely have a fairly constant diel profile. Combined with the evidence from the PTRMS tracers, we conclude that the most likely explanation for changing binPMF results is due to real atmospheric variation rather than an instrument artifact.

S8 Positive binPMF solution selection

In the positive binPMF solution with only three factors (Fig S7), species which peak either in the morning or evening but are not consistently high through the day or night are not captured well. The C18 species at *m/z* 306, 308, and 310 have high residuals, as do some species in the nighttime factor including *m/z* 312. Adding a fourth factor does a better job of accounting for this signal because distinct factors that peak either in the morning or evening are resolved. When a fifth factor is added (Fig S8), the alkylpyridinium *m/z* factor is split into two new factors. These new factors are very similar in their spectra with peaks at the same *m/z* and only minor differences in relative intensities. As with the splitting of the high *m/z* nitrate factor in the negative mode binPMF solution (described in Sect S4), one time series contains dips that correspond to spikes in the other time series, and the sum of the two is similar to the time series of the alkylpyridinium factor. Again, this appears to be splitting of a single factor into two new ones without any chemical significance. Therefore, the four-factor solution was selected.

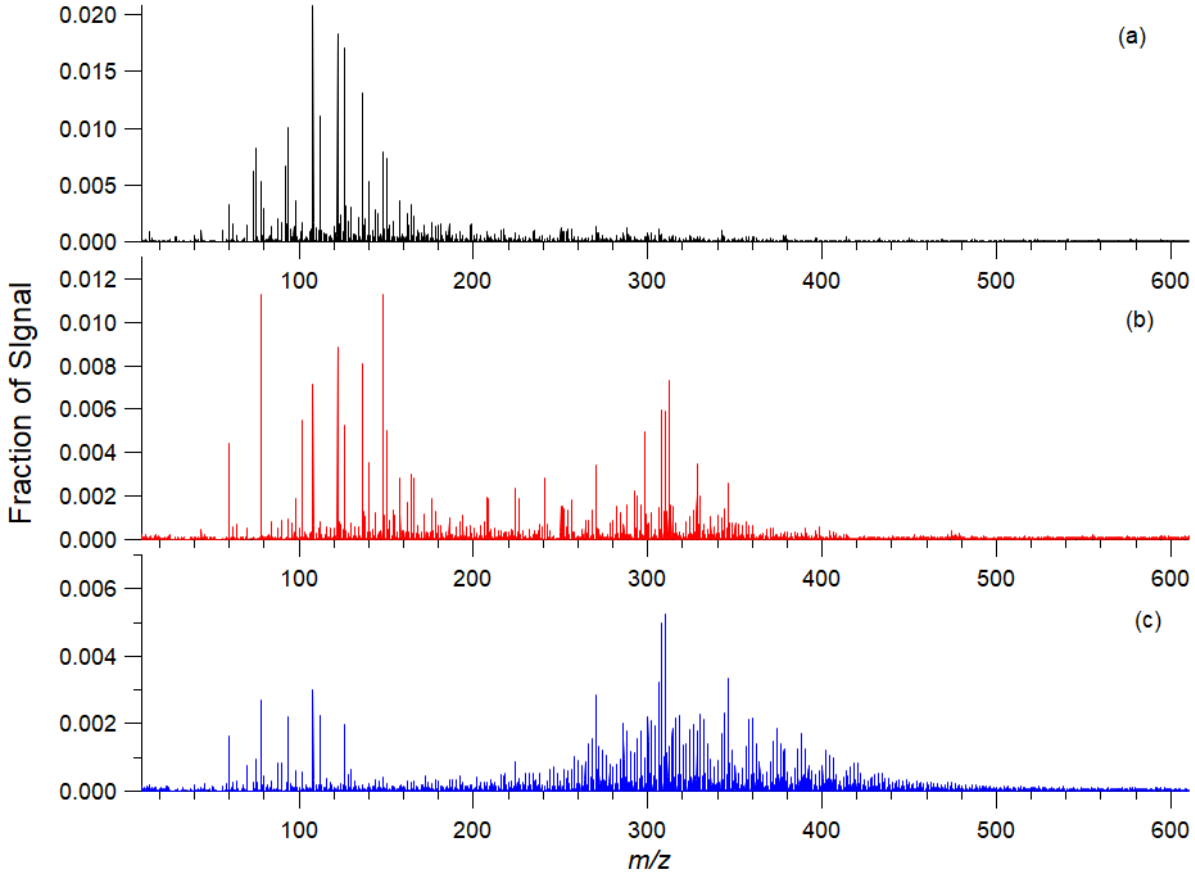

Figure S9: Mass spectra of the factors in the three-factor positive binPMF solution.

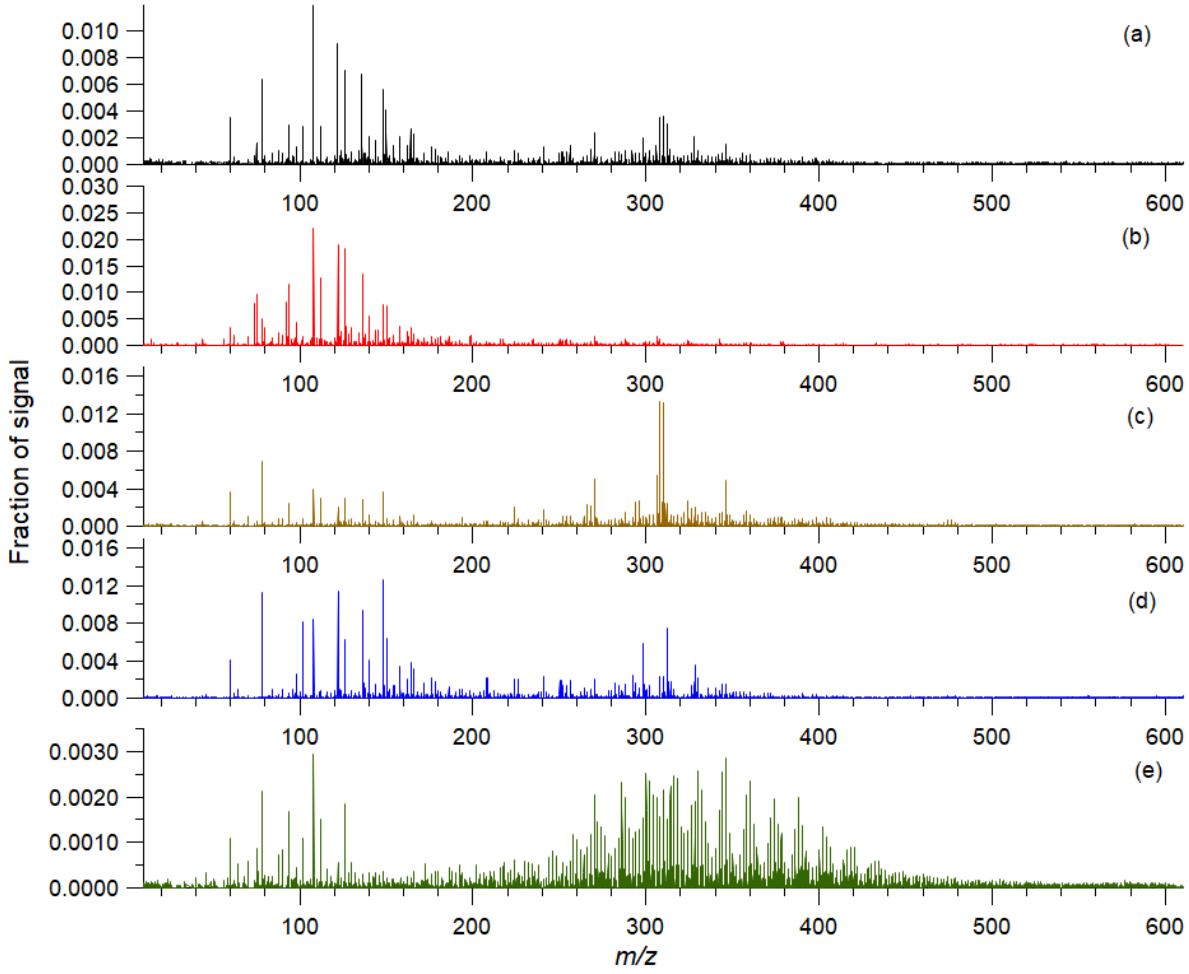

150 **Figure S10: Mass spectra of the factors in the five-factor positive binPMF solution.**

S9 Time series of positive binPMF factors and *m/z* 240

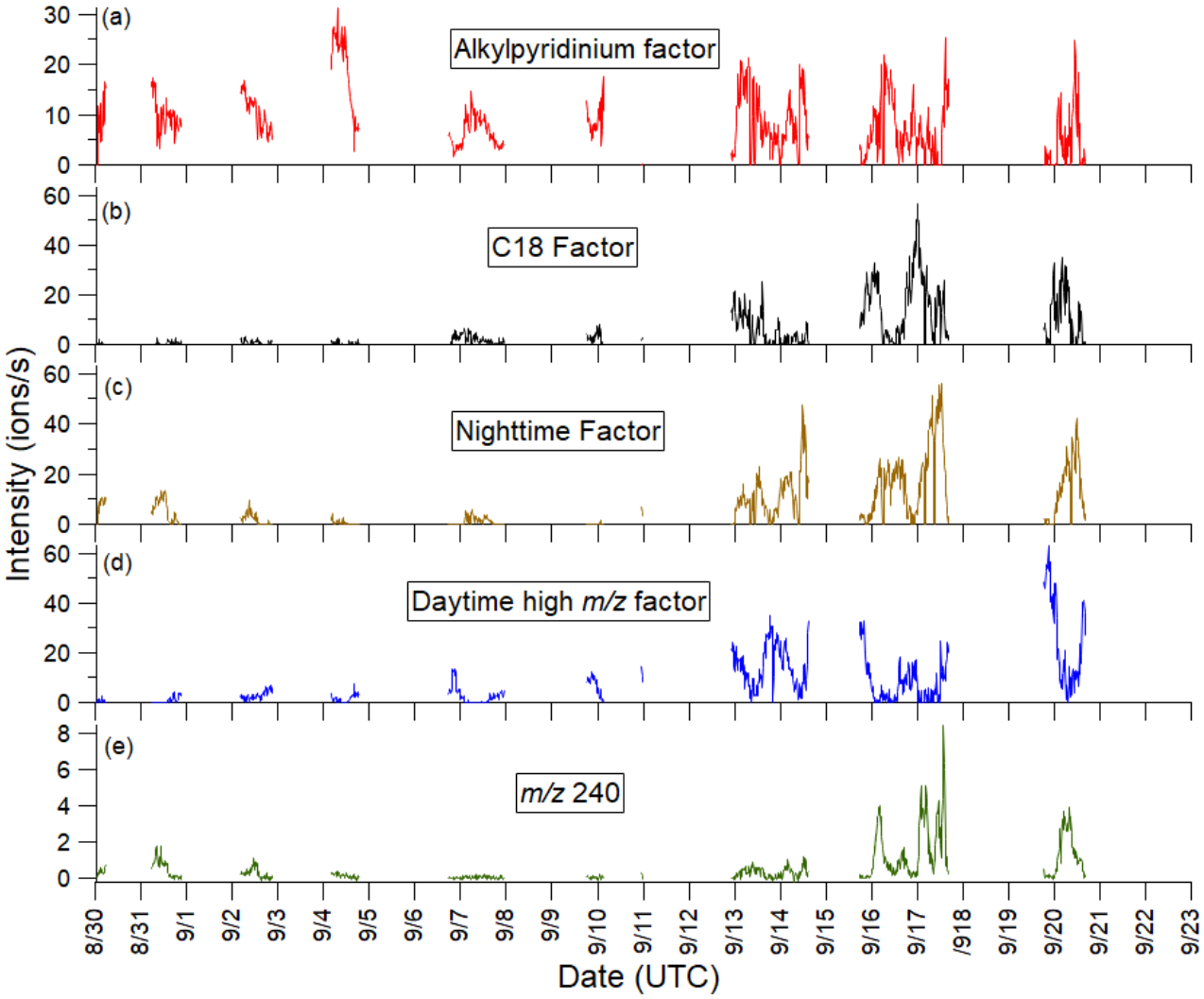

Figure S11: Time series of the four factors and selected ion in the positive binPMF solution (a) alkylpyridinium factor, (b) C18 factor, (c) nighttime factor, (d) daytime high *m/z* factor, and (e) the ion at *m/z* 240.

S10 Diel profiles of alkylpyridiniums

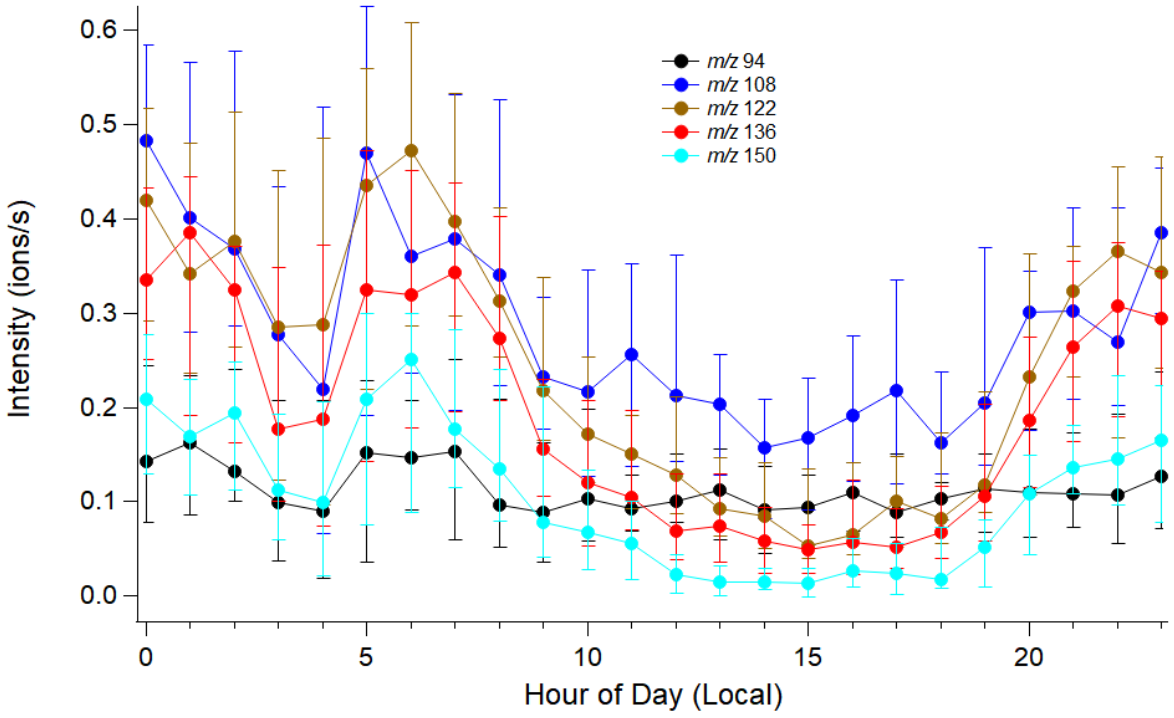

Figure S12: Diel plots of the series of five alkylpyridinium cations (*m/z* 94-150, $(C_5H_5(CH_2)_xN)H^+$, $1 \leq x \leq 5$) measured in positive mode.

S11 Diel profiles of C3 and C4 amines

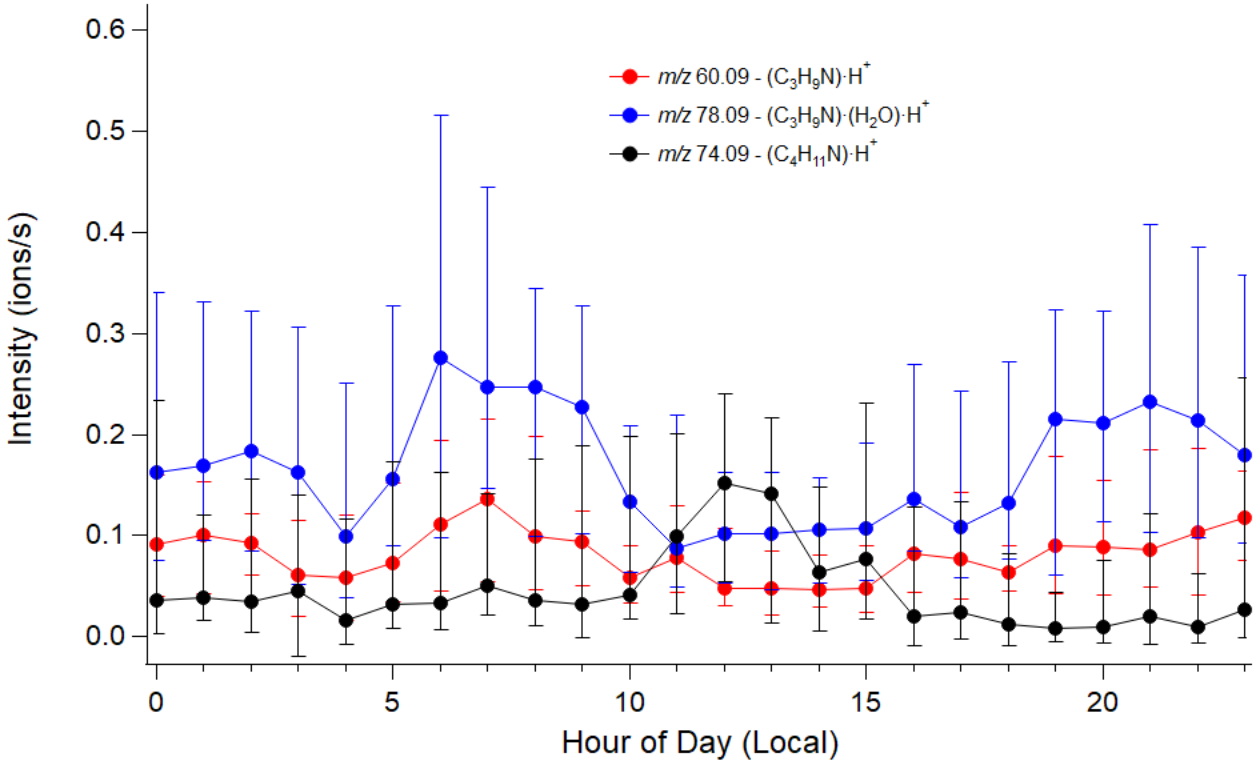

Figure S13: Diel plots of the bins containing C3 amine (C_3H_9N), C3 amine clustered with water, and C4 amine ($C_4H_{11}N$) signals. While the C3 amine and its water cluster peak early in the morning, the C4 amine is most intense in the middle of the day.

S12 Positive SKMD with possible formulas

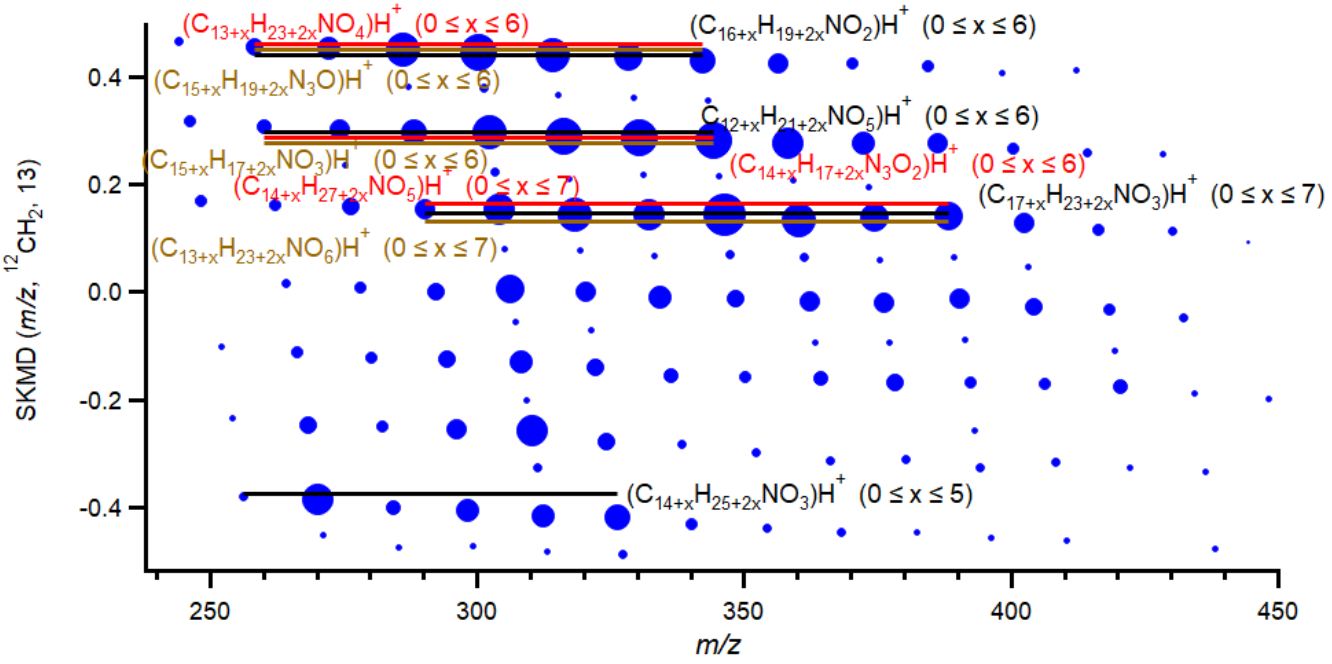

Figure S14: SKMD plot of high *m/z* daytime factor with CH_2 base unit and integer of 13. The most probable formulas are shown in black. Formulas in red and brown are considered less likely.

The SKMD plot of the high *m/z* daytime factor (Fig. S14) shows that some peaks fall along horizontal lines and are likely related by CH_2 units, but this does not hold true for all observed species. This result is confirmed by high-resolution peak fitting, which also suggests that the ions resulting in the observed peaks are not separated only by units of CH_2. For example, the two most intense peaks in the series of peaks with the highest scaled Kendrick mass defects (top line on the plot) are found at *m/z* 286 and 300. Since they are separated by Δ*m/z* of 14, it is possible that they are related by a CH_2 unit. Both the SKMD plot of binPMF peaks and high-resolution peak fitting suggest that $(C_{18}H_{23}NO_2)H^+$ and $(C_{19}H_{25}NO_2)H^+$ are reasonable formulas for these peaks. However, in the series of peaks with the most negative scaled Kendrick mass defects (bottom line of the plot) the most intense peak is at *m/z* 270. Both the SKMD plot and high-resolution peak fitting suggest that $(C_{15}H_{27}NO_3)H^+$ is a reasonable formula for this peak. There is a peak present at *m/z* 284, but the deviation of that point from the horizontal line implies that it is not related to the peak at *m/z* 270 by a CH_2 unit. High-resolution peak fitting confirms that $(C_{16}H_{29}NO_3)H^+$, the formula which corresponds to the addition of a CH_2 group, is not a likely formula for this peak. Therefore, both SKMD analysis and high-resolution peak fitting agree that the observed species are not related only by CH_2 units, and it is unlikely that the shift in the plot is an artefact caused by the binning and fitting procedure.

S13 Positive HYSPLIT back trajectory cluster analysis

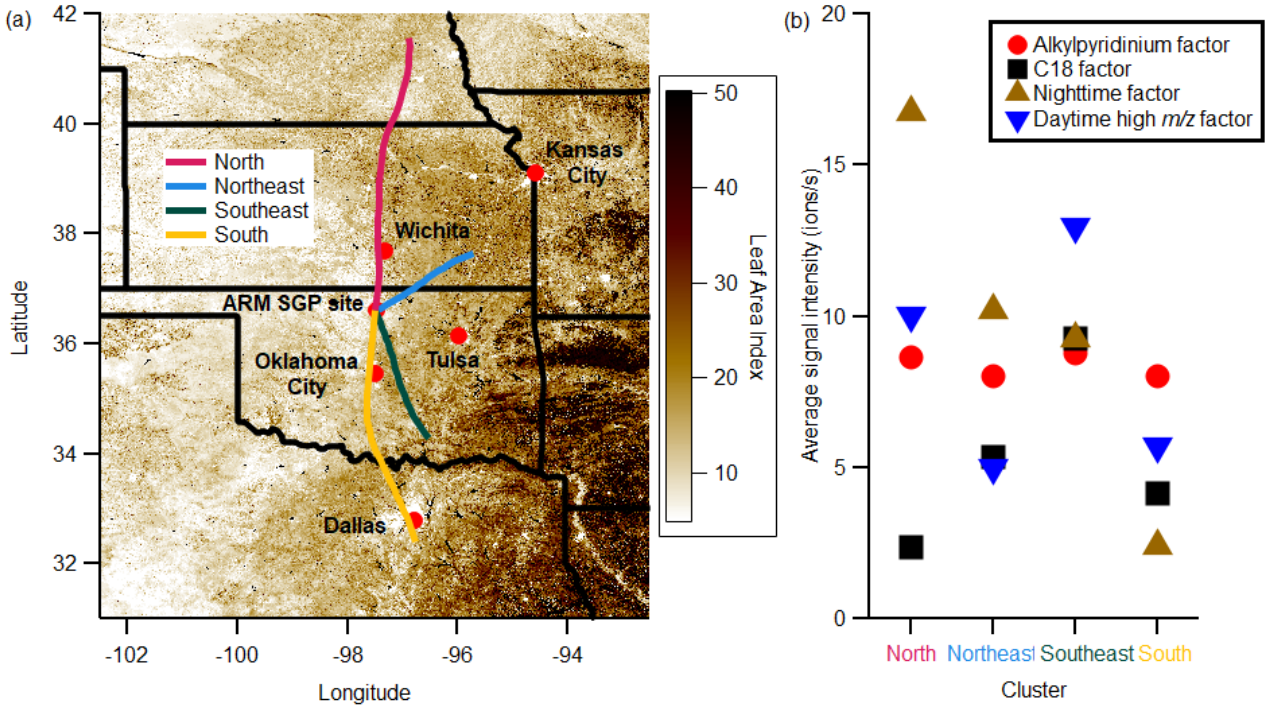

Figure S15: (a) HYSPLIT clusters calculated from back trajectories. The color scale shows leaf area index measured by MODIS. (b) Average signal intensities of factors for each HYSPLIT back trajectory cluster

As with negative factors, HYSPLIT back trajectory cluster analysis was performed for positive binPMF clusters. Figure S14 shows back trajectory clusters for 24-hour back trajectories calculated each hour overlaid on a map of leaf area index. Figure S14(a) shows the back trajectories grouped into each cluster. The north (n = 12 trajectories), northeast (n = 61), and southeast (n = 80) clusters respectively have 58%, 54%, and 48% of their trajectories arriving at the site during the day (8:00-18:00 local time). The south cluster (n = 54) is the only cluster which has a significantly different number of daytime and nighttime trajectories with 33% of trajectories arriving during the day.

Figure S14(b) shows the average signal of each binPMF factor when the HYSLPIT clusters arrive at the site. The alkylpyridinium factor is almost constant among the clusters, which is consistent with the long atmospheric lifetime expected for these species. This consistency could also be due to local sources distributed approximately uniformly around the site. For the other factors, interpreting the back trajectories is challenging since the sources and chemistry of the observed ions is not yet understood. Additionally, it should be noted that, especially for species with shorter lifetimes, local processes such as crop harvesting may contribute more to the changes in observed intensity than long range transport. Possible evidence that local emissions and chemistry may control these factors comes from the nighttime factor which is enhanced in the north cluster and

is lowest in the south cluster despite both of these trajectories passing over urban areas (Wichita, Kansas and Oklahoma City, Oklahoma respectively).

References

Mikkonen, S., Romakkaniemi, S., Smith, J. N., Korhonen, H., Petäjä, T., Plass-Duelmer, C., Boy, M., McMurry, P. H., Lehtinen, K. E. J., Joutsensaari, J., Hamed, A., Mauldin, R. L., Birmili, W., Spindler, G., Arnold, F., Kulmala, M., and Laaksonen, A.: A statistical proxy for sulphuric acid concentration, Atmos. Chem. Phys., 11, 11319–11334, https://doi.org/10.5194/acp-11-11319-2011, 2011.

Trojanowski, R.: Sulfur Dioxide Monitor (AOSSO2), 2016-08-23 to 2016-09-21, Southern Great Plains (SGP) Lamont, OK (Extended and Co-located with C1) (E13). ARM Data Center. Data set accessed 2020-07-10 at http://dx.doi.org/10.5439/1250820.

Zhang, D.: Radiative Flux Analysis (RADFLUXBRS1LONG). 2016-08-30 to 2016-10-01, Southern Great Plains (SGP) Central Facility, Lamont, OK (C1). ARM Data Center. Data set accessed 2020-04-23 at http://dx.doi.org/10.5439/1395069.